

PARTITIONING THE OUTBURST ENERGY OF A LOW EDDINGTON ACCRETION RATE AGN AT THE CENTER OF AN ELLIPTICAL GALAXY: THE RECENT 12 MYR HISTORY OF THE SUPERMASSIVE BLACK HOLE IN M87

W. FORMAN¹, E. CHURAZOV^{2,3}, C. JONES¹, S. HEINZ⁴, R. KRAFT¹, A. VIKHLININ^{1,3}

Draft version May 4, 2017

ABSTRACT

M87, the active galaxy at the center of the Virgo cluster, is ideal for studying the interaction of a supermassive black hole (SMBH) with a hot, gas-rich environment. A deep Chandra observation of M87 exhibits an approximately circular shock front (13 kpc radius, in projection) driven by the expansion of the central cavity (filled by the SMBH with relativistic radio-emitting plasma) with projected radius ~ 1.9 kpc. We combine constraints from X-ray and radio observations of M87 with a shock model to derive the properties of the outburst that created the 13 kpc shock. Principal constraints for the model are 1) the measured Mach number ($M \sim 1.2$), 2) the radius of the 13 kpc shock, and 3) the observed size of the central cavity/bubble (the radio-bright cocoon) that serves as the piston to drive the shock. We find an outburst of $\sim 5 \times 10^{57}$ ergs that began about 12 Myr ago and lasted ~ 2 Myr matches all the constraints. In this model, $\sim 22\%$ of the energy is carried by the shock as it expands. The remaining $\sim 80\%$ of the outburst energy is available to heat the core gas. More than half the total outburst energy initially goes into the enthalpy of the central bubble, the radio cocoon. As the buoyant bubble rises, much of its energy is transferred to the ambient thermal gas. For an outburst repetition rate of about 12 Myrs (the age of the outburst), 80% of the outburst energy is sufficient to balance the radiative cooling.

Keywords: galaxies: active - galaxies: individual (M87, NGC4486) - X-rays: galaxies

1. THE OUTBURST CHRONICLE OF M87'S SUPERMASSIVE BLACK HOLE

The cavities and shocks observed in cluster, group, and galaxy images of hot gas-rich systems chronicle the mechanical energy release, as distinct from the radiated emission, from supermassive black holes (SMBH) accreting at levels well below the Eddington mass accretion rate ($\dot{M}_{\text{Edd}} = 4\pi G m_p M_{\text{SMBH}} / \eta c \sigma_T$, M_{SMBH} is the SMBH mass, G is the gravitational constant, m_p is the proton mass, c is the speed of light, σ_T is the Thomson electron scattering cross section, and $\eta \approx 10\%$). For present epoch SMBHs in hot, gas-rich systems, the mechanical power dominates the radiated power (e.g., Churazov et al. 2000, 2005, Fabian et al. 2003, McNamara et al. 2005, Allen et al. 2006, Fabian 2012). The best, and often the only, way to derive the dominant energy release from the SMBH is through the effects of the SMBH on the surrounding hot atmosphere. The Eddington luminosity is given as $L_{\text{Edd}} = 1.3 \times 10^{47} (M_{\text{SMBH}}/10^9) \text{ ergs s}^{-1}$. With an SMBH mass of $3-6 \times 10^9 M_{\odot}$ (Harms et al. 1994, Ford et al. 1994, Macchetto et al. 1997, Gebhardt et al. 2011, Walsh et al. 2013), the Eddington luminosity of M87's SMBH is $L_{\text{Edd}} \sim 4-8 \times 10^{47} \text{ ergs s}^{-1}$. The currently observed bolometric radiative luminosity L_{rad} of the central AGN is $L_{\text{rad}} \approx 3 \times 10^{42} \text{ ergs s}^{-1}$ (e.g., Prieto et al. 2016). This L_{rad} is about five orders of magnitude lower than the Eddington limit for M87's mass, firmly placing the object into the category of low power AGNs. At the same time, the typical estimates of the jet mechanical power L_{jet} of the source are consistently higher, $\sim 10^{44} \text{ ergs s}^{-1}$ (e.g., Bicknell & Begelman

1996, Owen, Eilek and Kassim, 2000, Stawarz et al. 2006), implying that $L_{\text{rad}}/L_{\text{jet}} \sim 0.03$ or lower. All these properties suggest that we are dealing with a variant of a hot, radiatively inefficient flow (e.g., Ichimaru 1977, Rees et al. 1982, Narayan & Yi 1994, Blandford & Begelman 1999, Yuan & Narayan 2014). M87's spectral energy distribution also supports this conclusion (Reynolds et al. 1996; Di Matteo et al. 2003; Yuan et al. 2009; Moscibrodzka et al. 2016).

X-ray and radio observations of M87 chronicle AGN outbursts over the past 150 Myr. The VLA radio observations from Owen, Eilek & Kassim (2000; see also de Gasperin et al. 2012 observations with LOFAR) show evidence for the oldest outbursts (see Fig. 1b). The two filamented lobes lying NE and SW of the M87 nucleus have ages of $\sim 100-150$ Myr. An eastern "mushroom cloud" with stem and torus and a filamentary southwestern arm (Fig. 1b) have estimated ages of 40-70 Myr. X-ray filaments of cool gas (~ 1 keV) are seen coincident with these radio structures (compare Fig. 1a, b). In addition, there are several less prominent features including 1) a bubble that is separating from the central cocoon (the "bud") seen in both X-ray and radio images (see Fig. 1b and Fig. 2b), 2) a possible weak shock at about 5 kpc (about 10^6 years old; see Fig. 3), 3) a series of filamentary structures extending to the east that are likely the remnants of small bubbles (see Fig. 1a); 4) a large cavity/bubble to the east (beyond the radio torus labeled as "low-frequency bubble" in Fig. 1a⁵; and 5) gas sloshing cold fronts at large radii (33 kpc and 90 kpc; see Simionescu et al. 2010 for a detailed discussion).

Recent major outbursts, in the past 20 Myr, are seen in a combination of X-ray and radio imaging and are the focus of the present paper. The key features of these outbursts include:

¹ Smithsonian Astrophysical Observatory, Harvard-Smithsonian Center for Astrophysics, 60 Garden St., Cambridge, MA 02138; wrf@cfa.harvard.edu

² MPI für Astrophysik, Karl-Schwarzschild-Strasse 1, 85740 Garching, Germany

³ Space Research Institute (IKI), Profsoyuznaya 84/32, Moscow 117810, Russia

⁴ University of Wisconsin, Madison, Wisconsin

⁵ This large cavity/bubble is very clearly detected in the LOFAR images just to the north of the torus, see Figs. 7 and 8 in de Gasperin et al. 2012)

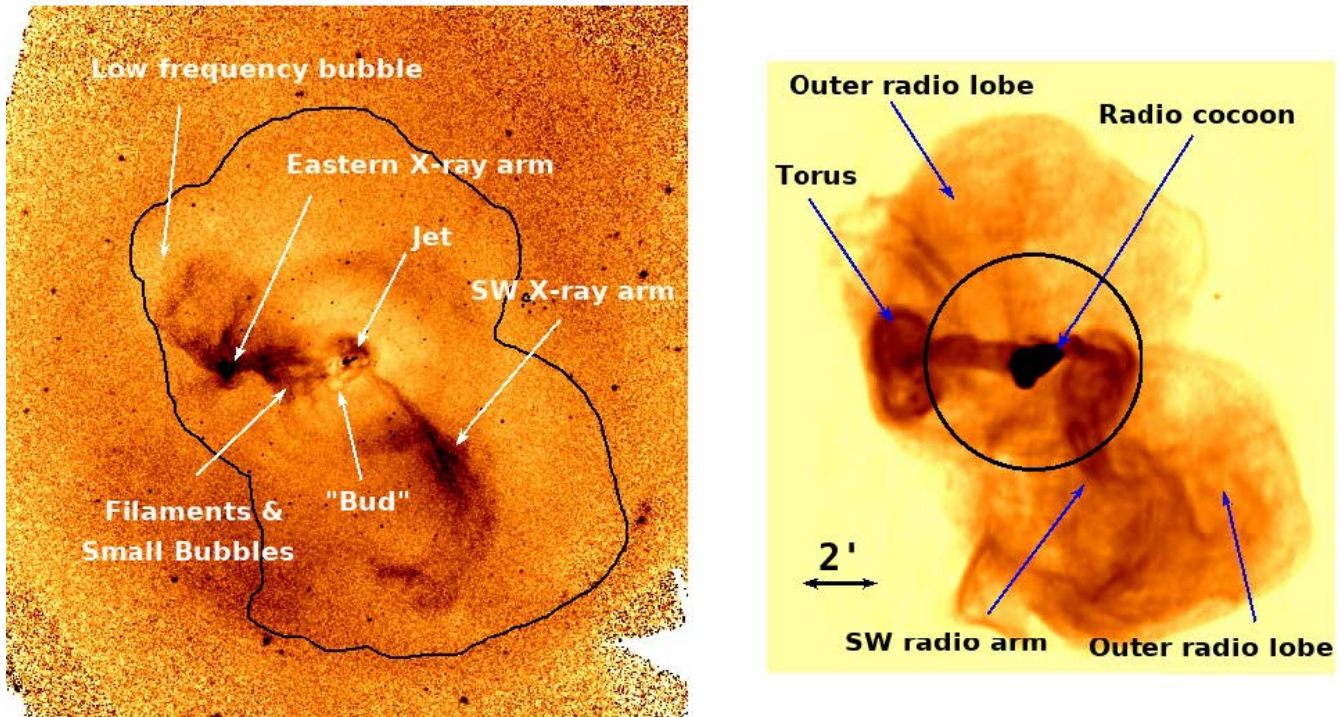


Figure 1. (a - left) The Chandra and 90 cm VLA (right) images, matched in scale, document the major outbursts from M87 (for details see Forman et al. 2007 and Owen et al. 2000). The Chandra image is a broad band image (0.5-2.5 keV) divided by the average radial profile to show faint surface brightness features. A contour of the faintest surface brightness regions of the radio emission (0.15 mJy per $1.5''$ sq. pixel) is shown in the X-ray image. At the very core, the X-ray image shows the M87 jet (extending $20''$ to the NW) which is filling the central cavity with relativistic plasma clearly seen as the very dark (saturated) region in the radio image. (b - right) The VLA image shows a pair of arms extending up to $5'$ to the east and southwest. The eastern arm appears as a torus atop a stem (a “mushroom cloud”) and represents a buoyant bubble of plasma that has risen about 20 kpc over the past 40-70 Myrs (Owen et al. 2000, Churazov et al. 2001). Only a twisted filamentary arm remains of the corresponding plasma bubble to the SW. X-ray filamentary arms of cool gas, uplifted by the buoyant plasma bubbles, are seen in the Chandra image. On the largest scales (extending to almost 40 kpc, two faint disk-like radio features are probably the remnants of the oldest outbursts from M87 (of order ~ 100 Myrs old; labeled as “outer radio lobe”). The X-ray image shows a brightness enhancement surrounding the large radio structures that is most clearly visible to the south. The X-ray image shows a shock at a radius of $2.8'$ (13 kpc; see also Fig. 2), which is represented in the radio image as a black circle, that was produced by a prominent outburst approximately 12 Myr ago.

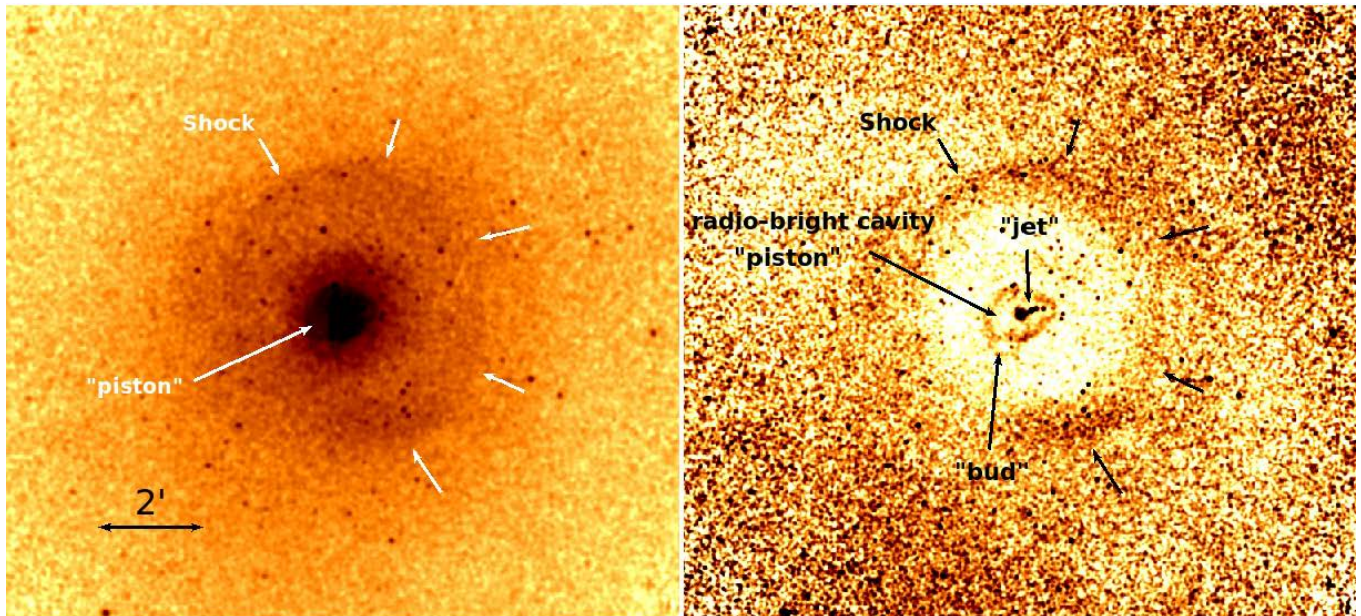


Figure 2. Two renderings of the hard band (3.5-7.5 keV) Chandra image of M87. As described in Forman et al. (2007; see also Churazov et al. 2016), the hard energy band is approximately the square of the pressure projected on the sky for gas temperatures of 1 - 3 keV. Images in this band show direct evidence for outbursts as over-pressured regions. The cool filamentary arms, so prominent in the softer band (Fig. 1 (left panel)), are not seen in the hard band. (a - left) The hard-band image with background subtracted and corrected for vignetting. (b - right) The image on the right shows the data divided by the average radial profile to “flatten” the field and enhance features in the bright core as well as showing the low surface brightness outskirts. The two panels show two clear outbursts – the 13 kpc ($2.8'$) primary shock, and the central, over-pressured cocoon with the X-ray bright rim, initially inflated when the current 13 kpc shock began and now re-pressurized by the current outburst.

- a classical shock at 13 kpc (2.8′) from the center of M87, seen in X-rays as a nearly complete azimuthal ring (Fig. 2 and Fig. 3). This was the first classical shock found in the hot gaseous atmosphere around a central cluster galaxy where both the gas density and gas temperature jumps at the shock could be accurately measured. As Forman et al. (2007; see also Forman et al. 2005, Million et al. 2010) showed, the density and temperature jumps are separately consistent with the Rankine-Hugoniot shock jump conditions (Rankine 1870, Hugoniot 1887) for a shock with a Mach number $M \sim 1.2$. The age of the outburst giving rise to the shock is about 12×10^6 years.
- the plasma-filled, radio-bright cocoon seen as an elongated bubble in the hard X-ray image (diameter $\sim 40''$) that served as the piston to drive the 13 kpc shock and is, most likely, now being re-energized by the present, ongoing outburst (see 2.7 and Figs. 1b, 2b, 5; also Hines et al. 1989).
- the prominent jet, observed over a very broad wavelength range, flaring knots, and variable gamma-ray emission (Hines et al. 1989; Owen et al. 2000; Marshall et al. 2002; Harris et al. 2003, 2006; Shi et al. 2007; Forman et al. 2007; Abdo et al. 2009; Acciari et al. 2010).

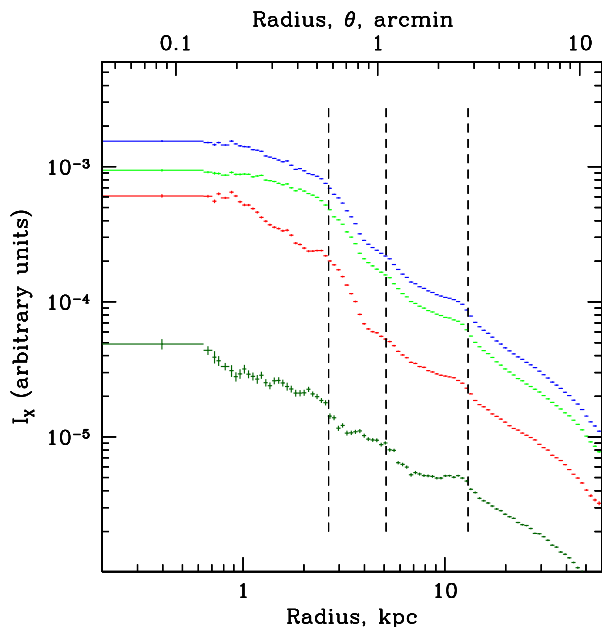


Figure 3. Surface brightness profiles in four energy bands: broad (0.5-3.5 keV), medium (1.0-3.5 keV), soft (0.5-1.0 keV), and hard (3.5-7.5 keV) from top-most to bottom-most. The surface brightness profiles are extracted from a 90° azimuth centered on north with point sources excluded and corrected for vignetting and exposure. The three dashed vertical lines indicate the locations of features seen in the pressure maps (Fig. 2). The inner most and outer most lines mark the strongest features and correspond to the current outburst that is re-inflating the central cavity and the 13 kpc shock. The 13 kpc shock is seen in all energy bands, while the central cavity is best seen in the hard band (lowest) surface brightness profile. A third weaker feature (possible shock) is seen at about $1' (\sim 5$ kpc; see also Forman et al. 2007, Million et al. 2010).

The prominent 13 kpc shock and its associated “piston” provide a unique opportunity to investigate the energy bal-

ance between shock heating and heating from buoyant bubbles inflated by AGN outbursts. Fig. 3 shows the signature of outbursts in the observed surface brightness profiles. Fig. 4 shows the same signatures in the deprojected density and temperature profiles. Fig. 4a is derived from the 360° azimuthal average and provides the cleanest estimate of the mean gas density properties, while Fig. 4b, a sector centered on North, where the surface brightness profile is least affected by the projection of cool filaments, provides the best estimates for the shock parameters (see Forman et al. 2007 for the derivation of the density and temperature jumps associated with the shock). This “clean” region in Fig. 4b shows the pronounced enhancements in both temperature and density at the 13 kpc shock (2.8′) and at the outer edge of the piston at $\sim 0.65'$ (~ 3 kpc).

We investigate M87’s recent outburst history by using a 1-D numerical shock model to characterize the observed properties including the gas temperature and density profiles. Because the outburst has occurred in the cool atmosphere of M87, compared to hotter atmospheres in more luminous clusters, we are able to derive the observable quantities of the outburst in considerable detail (see Forman et al. 2007, Churazov et al. 2008). By combining a simple model with the high quality observations of M87, we can determine the parameters of the outburst and the energy partition between the shock and the cavity enthalpy and thus help understand the different heating mechanisms required to suppress strong cooling flows in hot atmospheres in galaxies, groups, and clusters.

1.1. Cavity Size

One of the key constraints on the outburst model comes from the size/volume of the central cavity produced as the relativistic plasma from the jet displaces the hot X-ray emitting gas in the core of M87. The appropriate size to be used is complicated by the fact that the jet is double-sided and inclined to the plane of the sky. As a result, the jet is probably producing two cavities that together make an elongated structure rather than a single spherical cavity.

For a proper comparison with the predictions of the 1D model, it is important to estimate the bubble volume in 3D, since the PV work required to displace the X-ray emitting gas is the most direct proxy for the total energetics of the outburst in the model with “gradual” energy release (see Section 2.5 below). To this end, we have approximated the cavity as an inclined cylinder, co-aligned with the jet axis (Fig. 5). Projected on the sky, the cylinder consists of a circular cross section with radius $0.3'$ and height $1.1'$. Inclination angles for the M87 jet range from $10^\circ - 20^\circ$ (e.g., Biretta, Sparks & Macchetto 1999, Wang & Zhou 2009). Taking the volume as the geometric mean from the two extreme inclinations and converting this to a sphere gives a spherical volume with a radius of ~ 3 kpc (equivalent to $0.65'$). For our 1D model, we use this value in our calculations.

The X-ray cavity size matches that of the radio cocoon/bubble (Fig. 5) and we typically refer to the “cavity” in the discussion of the model.

2. SIMULATIONS OF THE M87 13 KPC SHOCK

Our simulations are carried out in the context of a simple outburst model that captures the key physics. The radio plasma, ejected from the supermassive black hole by the jet, inflates a central cavity, seen as lobes or a cocoon in M87 radio maps (Fig. 5, right panel). The inner radio lobes act as a piston that displaces the X-ray emitting plasma. Our results

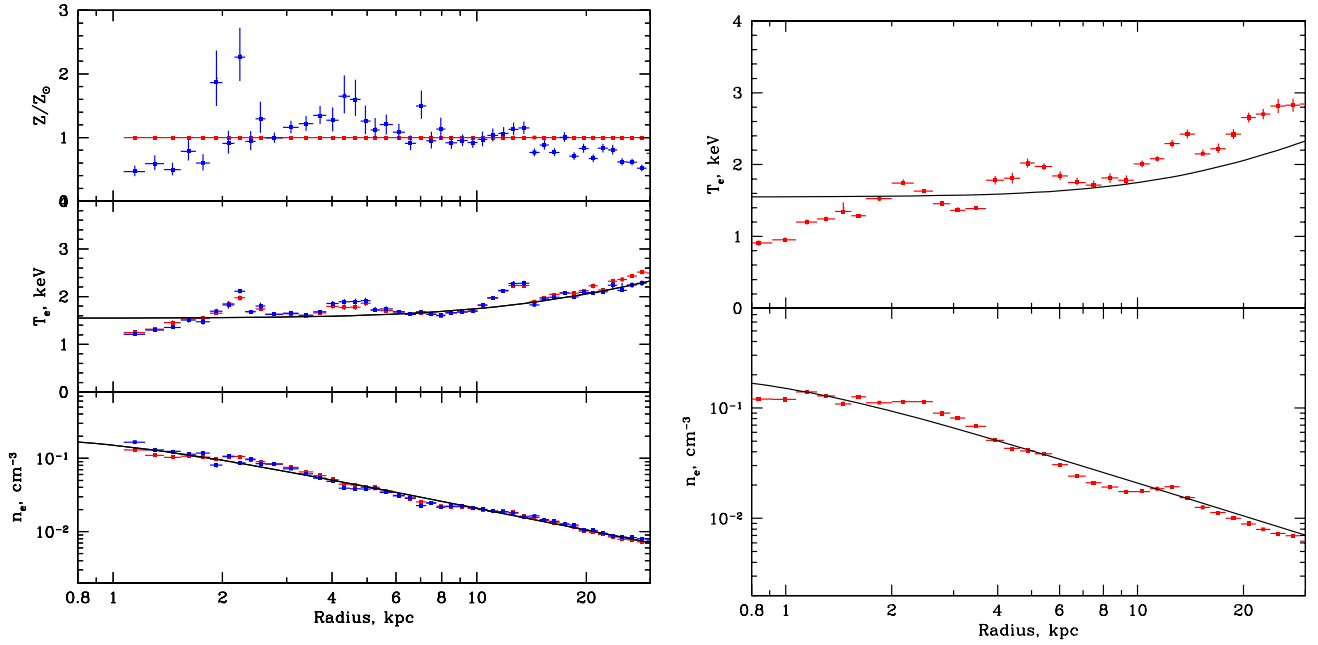


Figure 4. (a - left) The deprojected abundance, temperature and gas density profiles (red for abundance held fixed at solar and blue with variable abundance) derived from a full 360° azimuthally averaged radial profile (excluding the prominent cool clump that lies almost exactly at the shock radius within the eastern arm and that distorts the average temperature profile. Excluding all other arm-like features makes little difference to the average profiles.). The initial conditions are derived from fits to these data and are shown as the solid curves. These curves also serve, in later discussions, as proxies for the data themselves, for comparison to the models. (b - right) The deprojected gas density and temperature profiles derived from the 90° sector centered on North where the surface brightness profile is least disturbed by additional features, notably the soft X-ray arms. This “clean” region shows the pronounced enhancements in both temperature and density at the 13 kpc shock ($2.8'$) and at the outer edge of the piston at $\sim 0.65'$ (~ 3 kpc). The solid curves are the fits to the complete 360° azimuthally averaged profile that serve as the initial conditions. Spectral fits were done using an *apec* model and the deprojection procedure described in Churazov et al. (2008).

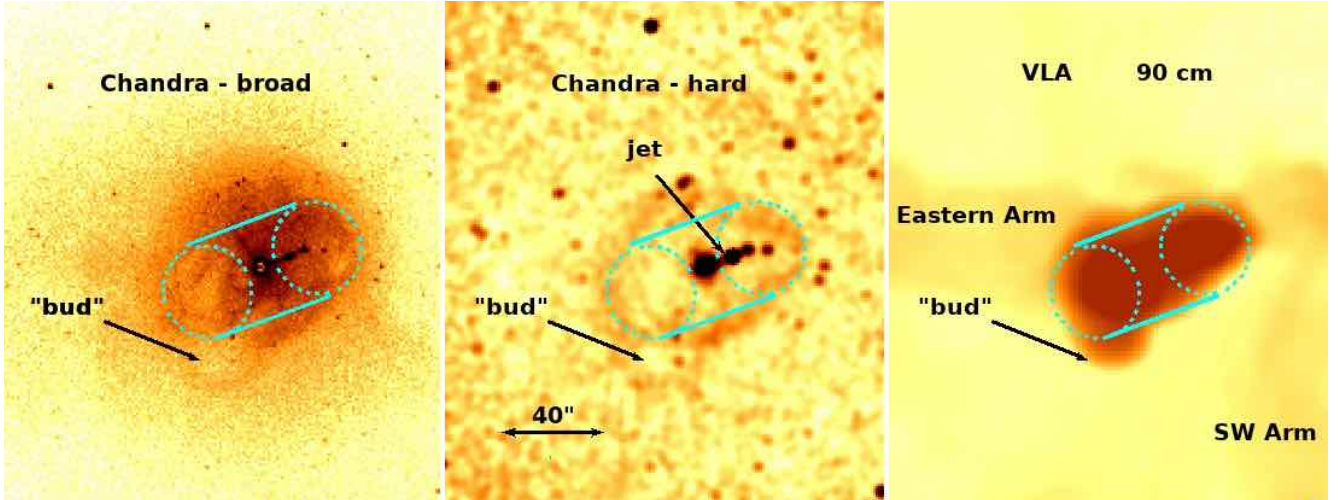


Figure 5. Images of the M87 core with the central cavity approximated as a cylinder (front and rear surfaces as dashed circles and sides as solid lines) with various features labeled. The three images of the core are: (left) Chandra broad band image (0.5-2.5 keV) divided by the average radial profile, (center) Chandra hard band image (3.5-7.5 keV) divided by the average radial profile, and (right) 90 cm VLA image of M87. The eastern and southwestern (SW) arms are very faint compared to the highly overexposed cocoon.

are uncertain due to projection effects arising from the unknown geometry and since we do not know the precise initial conditions of the M87 atmosphere, prior to these SMBH outbursts. Also, we neglect possible effects of diffusive processes on the weak shock (cf. Fabian et al. 2006). However, as we show, the qualitative features of the density and temperature profiles provide a robust characterization of the outbursts.

2.1. Numerical Modeling Details

We have performed a sequence of 1D Lagrangian numerical simulations of a shock propagating into the M87 atmosphere where we vary the energy deposited by the outburst and the timescale over which the energy is injected by the central AGN. The M87 atmosphere is assumed to lie in a static gravitational potential, $\phi(r)$, such that the observed gas density and gas temperature distributions (see section 2.2) are in hydrostatic equilibrium. We assume, for the initial conditions, that the present M87 gas density and temperature are close to those prior to the outburst, i.e., M87’s atmosphere is in a

“steady state” with repeated outbursts that are not unusually violent.

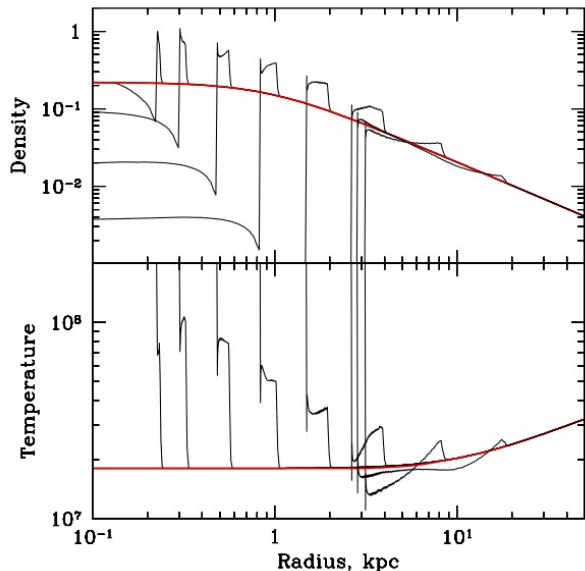


Figure 6. The gas density and temperature distributions of the fiducial model as a function of time. The shock is initially strong with both the gas density and gas temperature jumps decaying with time. The eight models shown are snapshots taken at 0.023, 0.061, 0.16, 0.41, 1.07, 2.77, 7.18, 18.6×10^6 years after the initial outburst. The particular model shown, with an outburst energy of 5.5×10^{57} ergs and a duration of 2.2×10^6 yrs, matches 1) the best fit Mach number ($M = 1.2$) at the 13 kpc radius of the observed shock and 2) the estimated central cavity (piston) radius of ~ 3 kpc. Since this model captures the key parameters of the outburst, it is referred to as the fiducial model. The initial conditions are shown as a solid red line (given in equations 1 and 2). The temperature interior to the piston reflects that for the mixture of very hot relativistic plasma that mixes with the small quantity of thermal gas present in the inner pixels of the model when the outburst begins.

We assume that an outburst from a SMBH deposits an energy E_0 uniformly over a time interval Δt . In the inner cells interior to the boundary of the piston (initially 0.2 kpc), the energy is deposited as a power law in radius to mimic the deposition of energy as a jet fills the central cavity (see Xiang et al. 2009 for additional details). For all gas components, we assumed in the actual calculations that $\gamma = 5/3$. For a cavity of radius R , pressure P (in pressure equilibrium with the ambient gas) and volume V , the minimum total energy required to inflate the cavity is $E_{tot} = \gamma/(\gamma - 1)PV$. Since the component interior to the piston is at least partially a relativistic plasma, the appropriate γ may be smaller and the input energy larger. For $\gamma = 4/3$ and subsonic expansion, E_{tot} would be 60% larger than for $\gamma = 5/3$. We discuss the implications of different values for γ in section 2.6.

2.2. Initial Conditions

The initial conditions of the hot gas surrounding M87 are a fundamental input to the model. Despite the high quality Chandra X-ray observations, the conditions of the atmosphere surrounding M87, as they appeared more than 10 Myrs ago, prior to the outburst are uncertain, since the gas surrounding M87 has experienced a variety of outbursts (and possibly even small mergers and the associated “gas sloshing”). However, as a dynamically old system with an old stellar population, we assume that the atmosphere around M87 is in quasi-equilibrium and has not undergone any dramatic changes in

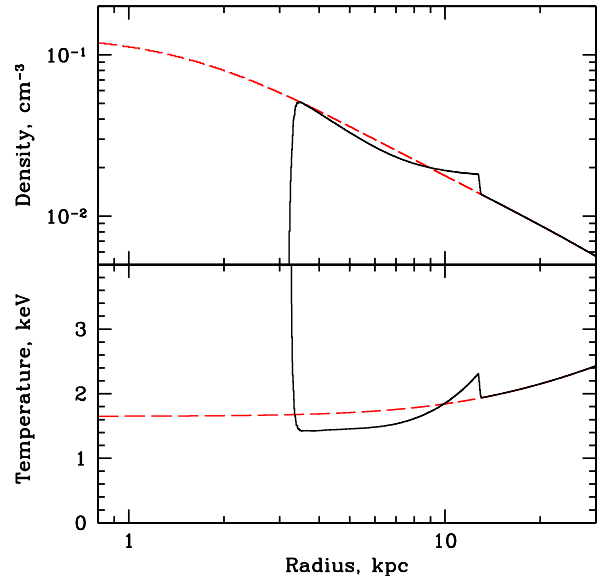


Figure 7. Initial radial profiles of density and temperature (the initial conditions) as modified by the outburst. The dashed red lines correspond to the initial conditions. The black solid lines show the density and temperature profiles that characterize the “fiducial 1D model” with total energy release 5.5×10^{57} ergs and outburst duration 2×10^6 yr, when the shock front is ~ 13 kpc from the center of the cluster. For the fiducial model (and for “long” outburst models in general), downstream from the shock, the gas temperature is lower than the initial temperature of the gas at the same radius (for reasons described in the text).

recent epochs. If, as seems likely, the SMBH in M87 is able to maintain a quasi-equilibrium between heating and radiative cooling, then the present is a “fair” match to the conditions that were present at the time of the outburst. Therefore, for the region interior to $6'$ (~ 30 kpc), we use the observed gas density and temperature distributions to derive the “unperturbed” gas density and gas temperature profiles that are fit to the deprojected data with the simple analytic functions:

$$n_e(r) = 0.22(1 + (r/r_c)^2)^{-3\beta/2} \quad (1)$$

$$kT(r) = 1.55(1 + (r/r_T)^2)^{0.18} \quad (2)$$

where $r_c = 0.2'$ (0.93 kpc), $\beta = 0.33$, and $r_T = 2.2'$ (10.2 kpc). These profiles, derived from the full 360° azimuthal average profile are shown in Fig. 4a and provide the initial baseline for the simulations. Fig. 4b shows the initial conditions compared to the observations of the northern sector where the shock is most clearly seen.

2.3. A Shock in the Atmosphere of M87

Applying our shock model to the initial conditions described above, we can examine a typical outburst. Our “fiducial” model with total outburst energy and outburst duration $E_{tot} = 5.5 \times 10^{57}$ ergs and $\Delta t = 2$ Myr has a temporal evolution shown in Fig. 6. This temporal evolution is characteristic of all the models. The initial shock weakens with time, because of energy dissipation at the front at early phases, when the shock is still strong, and undergoes pure spherical expansion at later phases. In the last snapshots, the shock is expanding at Mach $M = 1.2$ with amplitudes, in both density and temperature, that match the observations. The expansion of the central cavity (the piston) “stalls” at the present observed piston radius of about 3 kpc. In fact, the inertia of the accelerated gas ahead of the piston carries it beyond the pressure equilibrium radius and the piston radius subsequently decreases slightly

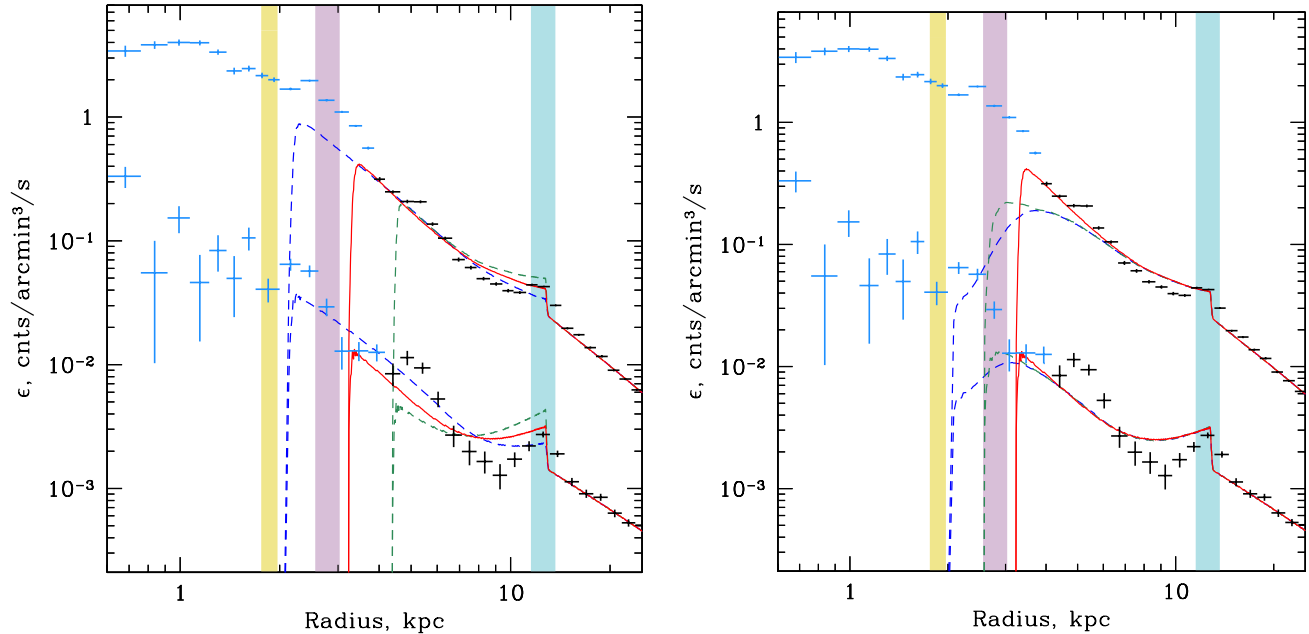


Figure 8. Comparison of outburst models with the data (the radial sector from 45-135°) for M87. The deprojected emissivity in two energy bands (upper data points are from 0.5-3.5 keV; lower data points are from 3.5-7.5 keV) is compared to i) models with varying outburst energy and fixed outburst duration (left panel) and ii) models with varying outburst durations and fixed outburst energy (right panel). The three vertical bands, from right to left, indicate the location of the shock (blue), “effective” cavity radius (estimated in section 1.1 after accounting for the line-of-sight projection) (magenta), and “apparent” cavity radius projected on the sky (yellow). The data points interior to the piston, within the region partially filled by the radio cocoon (radii less than about 3 kpc) are shown as light blue to indicate that they are dominated by systematic uncertainties including overlying complex structures, a highly uncertain deprojection (since the volume is partially filled with an uncertain amount of radio plasma), and should not be considered in comparisons to the model. The three models in the left panel have the same outburst duration, but different energies of 2.0, 5.5, 11×10^{57} ergs (violet, red, green) respectively, leading to different amplitudes of the shock. The three models in the right panel have, on the contrary, the same outburst energy of 5.5×10^{57} ergs, but different durations of 0.05, 0.56, and 2.2 Myr (violet, green, red), respectively, leading to different sizes of the central cavity. Thus the jumps in density/temperature and the size of the cavity together can naturally constrain the parameters of the outburst. The red curves in both panels correspond to the fiducial model that reproduces the major observables.

in the last time steps. This effect also is seen in the 3D simulation that we used to confirm the validity of our 1D models (described in section 2.9), but the effect is less pronounced. The final configuration, as we show below, matches the observations and for this reason, the outburst with $E_0 = 5.5 \times 10^{57}$ ergs and $\Delta t = 2 \times 10^6$ yrs is referred to as the fiducial model.

Fig. 7 shows the same fiducial model at the moment when the shock front reaches 13 kpc, corresponding to the observed shock radius. For the fiducial model (and for “long” outburst models in general), downstream from the shock, the gas temperature is lower than the initial temperature of the gas at the same radius. This is due to a combination of two effects. First, the rarefaction region behind a shock is a generic feature of weak spherical shocks (as described by Zeldovich & Razier 2002 and Landau & Lifshitz 1959). Second, in these models, the adiabatic expansion of the gas that is displaced from its initial location to lower pressure regions (larger radii) contributes to the temperature decrease. These features can be identified in many of the figures in this paper.

The lack of perfect spherical symmetry, the presence of cool structures (arms), and the uncertainty in the initial conditions complicate any detailed, quantitative comparison of the model and data. However, a qualitative (“factor of 2”) comparison is possible. Since the wedge to the North is less contaminated by cool structures, except for the inner 45”, we used the deprojected emissivities in the 0.5-3.5 and 3.5-7.5 keV bands for comparison with the model predictions (see Fig. 8). The emissivity in these two energy bands was calculated using the predicted density and temperature profiles assuming fixed solar metallicity. For the models shown in Fig. 8, the fiducial model

captures the key parameters measured for the M87 outburst and matches the size of the central cavity, the observed radius and strength of the shock (in both density and temperature), and the emissivity outside the central cavity.

As noted above, none of the 1D models provides a “perfect fit” to the data over the entire radial range. This is especially true for the innermost part, where the 1D model predicts the complete evacuation of the gas as it is pushed away by a spherical piston. In a real cluster, the gas is expected to be evacuated only from regions occupied by the cavities (the radio plasma), while the thermal gas can still be present along other directions. This is why we will compare the size of the cavity predicted by the 1D simulations to that derived in section 1.1, rather than directly comparing the predicted and observed profiles. For the shock front region, which is farther away from the center, the effects of asymmetry should be less severe and the direct comparison of the radial profiles is better justified.

2.4. Effects of Outburst Energy and Outburst Duration

To explore the range of allowed outburst parameters, we separately investigate the effects of varying the outburst energy and outburst duration. These two parameters govern the final outburst configuration.

For a given outburst duration, the outburst energy strongly affects the amplitude of the shock. Fig. 9a shows the gas density and temperature when the shock reaches 13 kpc, for outburst energies of 1.4, 5.5, 22×10^{57} ergs. The choice of outburst energy brackets the energy described above as the fiducial value. As Fig. 9a shows, the amplitude of the shock alone

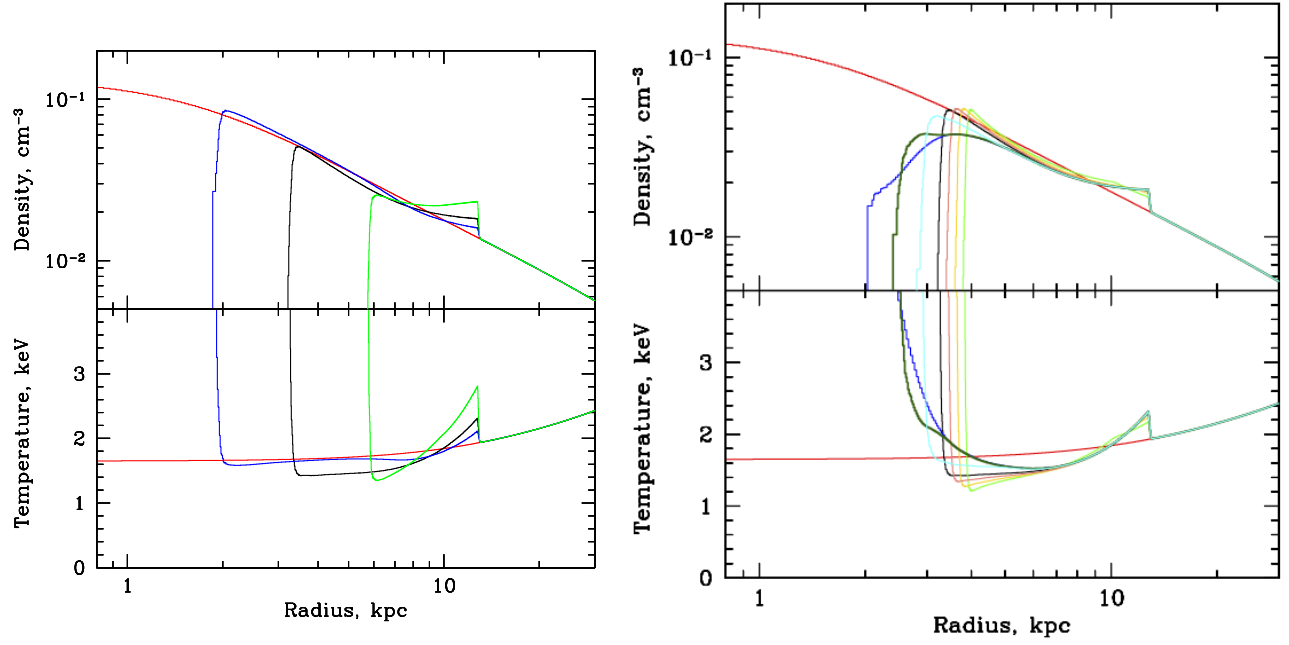


Figure 9. (a-left) For an outburst duration of 2.2×10^6 yrs, the fiducial value, we show a series of models with outburst energies of 1.4, 5.5, 22×10^{57} ergs when the shock lies at a radial distance of 13 kpc and hence having different ages). As the models show, the outburst energy is the major contributor to the amplitude of the shock. (b-right) For an outburst energy $E = 5.5 \times 10^{57}$ ergs, we show a set of models when the shock has reached a radius of 13 kpc for outburst durations of 0.1, 0.4, 1.1, 2.2, 3.1, 4.0, 4.4, 6.2×10^6 yrs. The magnitude of the shock is independent of duration for durations less than about 4×10^6 yrs. For longer duration events, the cavity is still significantly over-pressurized. As shown in Fig. 12, the duration is constrained by the combination of shock strength and piston/cavity size.

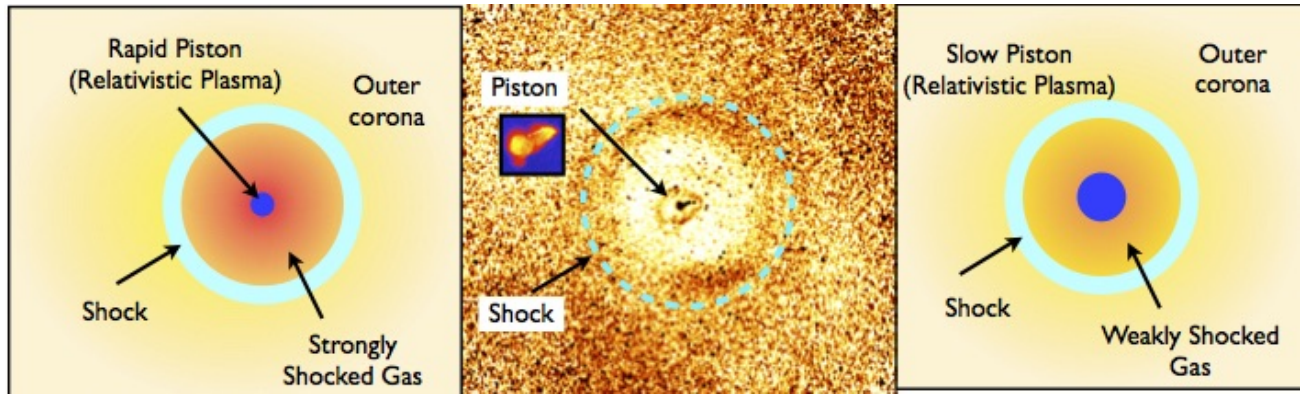


Figure 10. Schematic of the two shock scenarios - a short and a longer outburst. The modeled gas density and gas temperature profiles are shown in Fig. 11. **(a - left)** A powerful, short duration outburst ($\Delta t = 0.1 \times 10^6$ yrs) drives a strong shock into the surrounding atmosphere. At the present time, the region interior to the shock (located at the observed 13 kpc radius) would enclose a central hot, strongly shocked, low density atmosphere. **(b - center)** X-ray image of M87 divided by the average radial profile to better show the central piston and the jet with an inset image of the 6 cm radio emission that shows the piston that drove the M87 outburst. The dashed blue circle (labeled “Shock”) indicates the outer edge of the shock which is seen as the bright ring of emission. **(c - right)** A longer duration outburst, ($\Delta t = 2.2 \times 10^6$ yrs; the fiducial model) provides the same magnitude shock at 13 kpc, but only weakly shocked gas interior to the shock location and a larger central plasma-filled, piston. As discussed in the text, short duration outbursts are inconsistent with the observations.

provides a direct diagnostic of the outburst energy. Also, note that the different values of the outburst energy yield different sizes for the central piston – larger energy outbursts drive stronger shocks that reach 13 kpc in a shorter time and have larger central cavities of relativistic plasma.

We also have investigated the effects of varying the outburst duration. Fig. 9b shows the gas temperature and gas density profiles for models with the outburst energy held fixed at $E_0 = 5.5 \times 10^{57}$ ergs and with outburst durations ranging from 0.1 to 6.2×10^6 yrs. While the amplitude of the shock at 13 kpc varies only slightly, the size of the piston varies dramatically. The models show the characteristic behavior of “short” and “long” duration outbursts. As we show below, by matching the observations to the models in more detail, we can estimate a quantitative value for the outburst duration. Also, as Fig. 9b shows, a “short” duration outburst produces a central region with $\sim 2-3$ kpc radius), starting just beyond the outer boundary of the piston, that consists of hot, low density gas. In contrast, the longer duration, initially weaker shocks, with the same total outburst energy, are bounded by cool shells and have no extended hot, shocked region (see also Brighenti & Mathews 2002).

Thus, the combination of Fig. 9a and 9b shows that the outburst energy is determined (primarily) by the magnitude of the jumps.

2.5. Short and Long Duration Outbursts

To further illustrate the principles that drive the models described here and how the duration of the outburst affects the appearance of the hot corona, we select two examples that illustrate the effects of the outburst duration on the properties of M87 – a short duration outburst and a longer duration outburst. The short duration outburst has a duration $\Delta t = 0.1 \times 10^6$ yrs while the longer duration outburst has $\Delta t = 2.2 \times 10^6$ yrs (the blue and black curves in Fig. 9b). Fig. 10 shows graphically the dramatic difference that may arise from the two different duration outbursts.

Quantitatively, the different characters of the short and long outbursts are shown in Fig. 11a where we label the different regions that characterize the different types of outbursts. We show the gas density and gas temperature profiles of the 0.1×10^6 yr duration outburst (blue) and the fiducial 2.2×10^6 yr duration outburst (black). We have labeled the

key regions – the piston, the hot, low density shocked envelopes (blue text) for the short duration outburst and the piston and the cooler, denser envelope for the fiducial duration outburst (black text). Although the physics of the outbursts are identical, the duration imprints a qualitatively different signature on the surrounding atmosphere with quite different over-pressures and Mach numbers as a function of time (see Fig. 11b). For a given shock strength, the longer outburst produces a larger cavity, by a factor of three in volume, that can be used as a proxy for the outburst duration.

The models are shown at the time when the modeled shock reaches 13 kpc. For the two example outbursts (0.1 and 2.2 Myr durations) considered in Fig. 11, the outburst ages (time for the shock to reach 13 kpc) change by only about 10% (11 vs. 12 Myr for the 0.1 and 2.2 Myr durations). Despite the large difference in initial Mach number (Fig. 11b) for the outburst energy (5.5×10^{57}) that yields density and temperature jumps consistent with the observations, the age is dominated by the late phases as the shock approaches 13 kpc.

Also, longer outbursts could be characterized by the absence of a hot, low density envelope around the central cavity that is filled with relativistic plasma. Such an envelope, characteristic of short outburst models, is formed by the gas that has passed through the strong shock. The lack of such an envelope in the data is consistent with the “long outburst scenario”. Whether it can be used as a strong argument against the short outburst model depends on the efficiency of thermal conduction in the gas, which is an open issue.

2.6. The Fiducial Model - a single outburst model for the 13 kpc shock

To quantitatively bound the family of outburst parameters, we examine an ensemble of shock models where we have varied the outburst energy and duration. As described above, we first simulate the primary outburst that produced the 13 kpc shock and assume, for this initial comparison of observations to models, that this is the only outburst that affects the inner 13 kpc of M87. Our outburst model is characterized by two key outburst parameters - the duration (we assume constant power during the outburst event) and the total energy deposited.

The parameters we must match are (a) the shock jump conditions which, as noted above, primarily determine the total

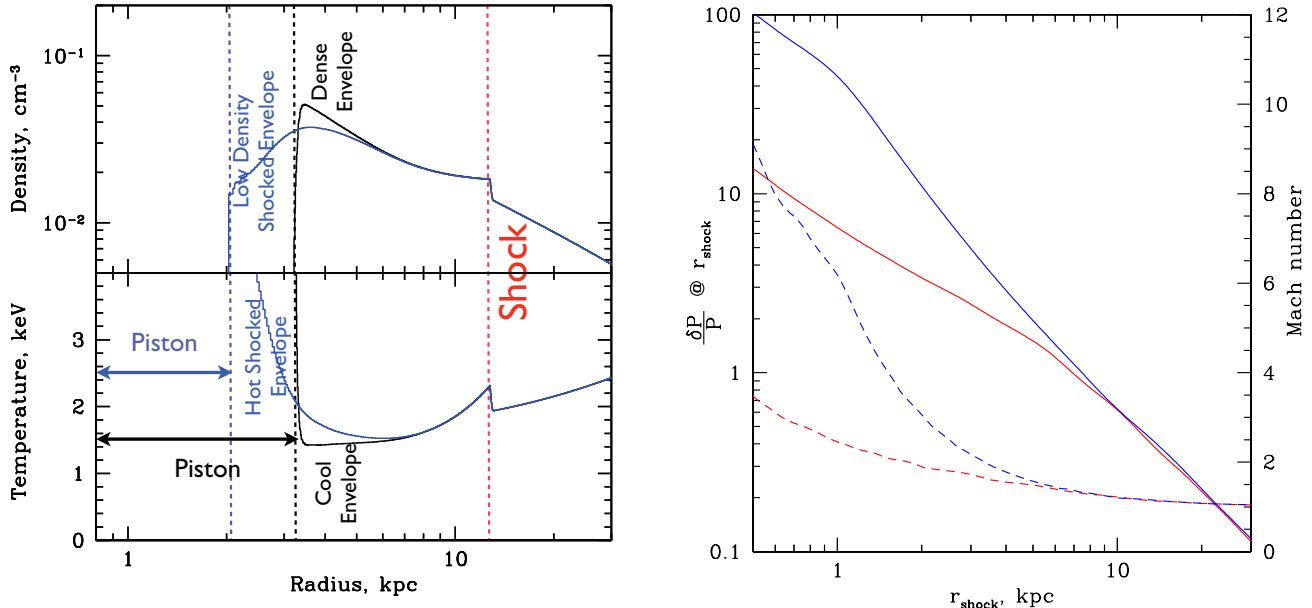


Figure 11. (a - left) The gas density and gas temperature profiles resulting from two outbursts - one with a “short” of 0.1 Myr duration and a second with a 2.2 Myr duration (the fiducial model) (blue and black curves respectively). The models are shown at the times that the modeled shock reaches 13 kpc, the radius of the observed shock. These times are 11 and 12 Myr, for the shorter and longer/fiducial duration outbursts, respectively. The dashed lines (blue and black) indicate the outer radii of the piston that created the shock (marked with the red dashed line at 13 kpc). The piston from the short duration outburst is surrounded by a low density, hot shocked envelope. The longer duration outburst (the fiducial model) is instead surrounded by a dense, cool envelope. At radii near the shock, the densities and temperatures of the two models are nearly identical. (b - right) The evolution of the shock strength, parameterized as the pressure jump for the short and longer duration models. The pressure jump for outbursts of duration 0.6 Myr (blue, solid curve) and 2.2 Myr (red, solid curve) with outburst energy of 5.5×10^{57} ergs is shown as a function of radius. The pressure jumps for the two models differ dramatically at small radii where the Sedov-like outburst yields a much stronger over-pressure. As the shocks evolve, they both match the observed shock at 13 kpc, but the Sedov-like outburst leaves a residue of hot, strongly shocked gas as shown in panel (a). For both outbursts, the equivalent Mach numbers are shown as dashed lines with axis on the right. The upper dashed line (blue) is for the 0.6 Myr duration outburst and that for the 2.2 Myr outburst is the lower dashed (red) curve.

outburst energy (E_{tot}), and (b) the radius (r_p) of the radio cocoon, the piston driving the shock, and (c) the observed radius of the 13 kpc shock. We could use either the temperature jump or the density jump to constrain the model. The density jump is statistically more accurate but has a systematic uncertainty associated with the steep density gradient arising from the “cool core” atmosphere surrounding M87. The temperature jump is less accurate statistically but may provide a more realistic measure of the uncertainties inherent in the complex atmosphere of M87. Mach numbers derived for the density and temperature jumps are fully consistent (see Forman et al. 2007). For the purpose of constraining the model parameters, we choose the less constraining temperature jump to better allow for the systematic uncertainties.

Fig. 12 is a grid of models for two parameters – the outburst energy, E_{tot} and the outburst duration, Δt . Loci of equal shock temperature jump (blue) and equal cavity size (red) are drawn. The value of the gas temperature jump is $kT_{\text{shock}}/kT_{\text{initial}} = 1.18 \pm 0.03$ (Forman et al. 2007). The second constraint arises from the size of the central cavity, the piston. We identify the piston with the central radio cocoon which is labeled in the X-ray image shown in Fig. 10b (central panel) as well as in Fig. 1b and 2b.

As noted above and shown in Fig. 12, for outburst durations less than about 3 Myr, the outburst energy is *independent* of outburst duration (i.e., the loci of equal density jumps are nearly vertical). For durations longer than 3 Myr, the acceptable range of energies does depend on the outburst duration.

The second constraint, the radius of the central cocoon, is derived from the X-ray and radio images (see Fig. 5 as discussed in section 1.1). The intersection of the radius and den-

Table 1
Fiducial Outburst Model in M87

Outburst Age (Myr)	12
Outburst Duration (Myr)	~ 2
Outburst Energy (10^{57} ergs)	~ 5
Energy carried by shock	$\lesssim 22\%$
Thermal energy in cavity	$\sim 27\%$
Change in gravitational energy	$\sim 40\%$
Energy in shock heated gas	$\sim 11\%$
Energy available for heating	$\sim 80\%$

sity constraints indicates the most probable locus of points of (energy, duration) for the outburst. The center of this region is $E_{\text{tot}} \sim 5.5 \times 10^{57}$ ergs and $\Delta t \sim 2$ Myr.

With the known properties of the surrounding atmosphere and the derived outburst details, we can compute the present epoch energy partition arising from the outburst (Table 1; see also Tang & Churazov (2017) who ran a set of models with varying durations and energetics in a homogeneous medium to determine the energy partition and then mapped the results to more realistic density/temperature profiles.) For the fiducial outburst of 5.5×10^{57} ergs, approximately 11% of the energy resides in the kinetic energy of the shock (and a comparable amount in the thermal energy of the shock, since the shock is weak) that can be carried away from the central region to larger radii since the shock is now relatively weak. At least 50% (and as much as 64%) of the energy is contained in the enthalpy of the central cavity/piston, and about 11% of the energy has been transformed into heating the gas as the

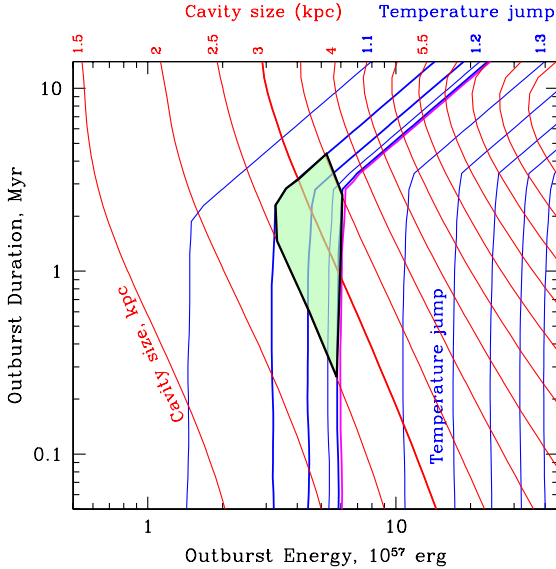


Figure 12. A grid of models as a function of outburst energy and outburst duration, for a one dimensional outburst model. The model parameters are taken at the time when the modeled shock reaches 13 kpc, the radius of the observed shock. Within this grid of models, we draw lines of constant temperature jump ($kT_{\text{shock}}/kT_{\text{initial}}$; blue solid lines) and constant piston size (radio cocoon; red solid lines). The values of the temperature jump and piston size are labeled along the top axis of the figure in the corresponding color. The green region indicates the intersection between regions defined by $kT_{\text{shock}}/kT_{\text{initial}} = 1.18 \pm 0.03$ and cavity size of 3 ± 0.5 kpc.

shock moved outward to its present position. In summary, in the fiducial model, about 30% of the outburst energy is deposited in the shock. In the model, about 10% of this energy has already been dissipated into heat as the shock traversed the region interior to its present 13 kpc location.

Our 1D simulations assume the adiabatic index $\gamma_g = 5/3$ for the gas inside and outside the “piston”. If, in fact, the energy density inside the piston is dominated by relativistic plasma with $\gamma_r = 4/3$, the thermal energy inside the cavity $\sim \frac{1}{(\gamma-1)}$ has to be increased by the factor $\frac{\gamma_g-1}{\gamma_r-1} = 2$ (see Table 1), while keeping all characteristics of the gas outside the piston unchanged. This would correspond to a moderate increase of the total energy, required to inflate the bubble, and also a reduction in the fraction of energy that goes into the initial shock.

Enthalpy of the Central Bubble – The central bubble, the radio-emitting cocoon, contains a large fraction of the total outburst energy. Much of the enthalpy in a central bubble is available for heating of the central region where radiative cooling is important (e.g., see Churazov et al. 2001, 2002; see also Nulsen et al. 2007). The fractional energy, f , retained by the buoyantly rising bubble with adiabatic index γ , is given as $f = (p_1/p_0)^{(\gamma-1)/\gamma}$ as the pressure changes from p_0 to p_1 . For a relativistic plasma bubble, $\gamma = 4/3$ and for a non-relativistic plasma, $\gamma = 5/3$. Fig. 13 shows the energy retained by a rising bubble in M87’s atmosphere using the fitted density and temperature profiles given in equations 1) and 2). The enthalpy of the buoyant cocoon is dissipated into a variety of forms including internal waves, sound waves, turbulent motion in the wake of the bubble, potential energy of uplifted (cool) gas, and large scale bulk flows. While sound waves can carry energy away from the central region, most other channels would eventually result in heating the central

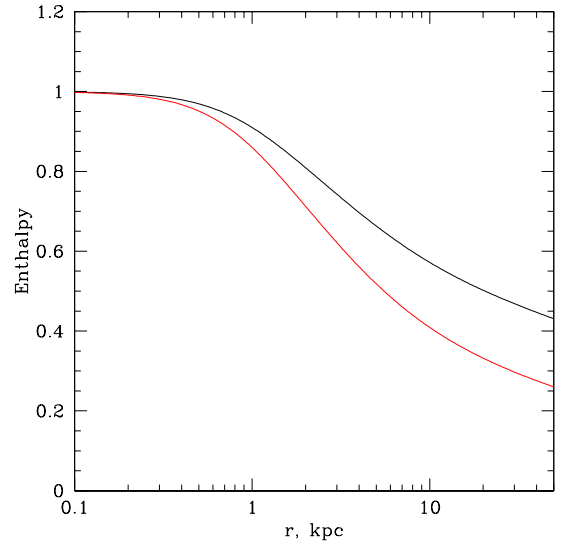


Figure 13. For a buoyantly rising bubble, the fractional enthalpy loss for a plasma with adiabatic indices of 5/3 and 4/3 (upper and lower curves, respectively). Buoyant plasma bubbles rising from the galaxy center to about 20 kpc, would lose approximately 50% of their initial enthalpy which would ultimately be converted into thermal energy of the X-ray emitting plasma on a timescale that depends on the plasma microphysics.

region (see Churazov et al. 2001 for a more detailed discussion on the containment of SMBH outburst energy in the core region). As Fig. 13 shows, a buoyant bubble rising to about 20 kpc in M87’s atmosphere would lose about 50% of its enthalpy. This energy will eventually be dissipated into heat on a time scale that depends on the plasma microphysics.

2.7. Multiple Outbursts

The outburst that generated the 13 kpc shock is likely not the most recent one from M87’s SMBH. As the hard band images Fig. 1b and 2b show, there is a surface brightness enhancement surrounding the radio cocoon (the central bubble) indicating that the cocoon is an overpressurized region which is being driven by the current outburst we see in M87 – that also drives the existing jet.⁶ To understand the effects of the more recent outburst on our derived shock parameters, we add a second ongoing outburst at the present epoch to provide the observed overpressure within the central cocoon.

The current (ongoing) outburst has an energy (up to the present) of 2×10^{57} ergs (determined by the weak density jump at ~ 3 kpc) and a duration of about 1 Myrs. If we include this recent outburst, the age of the main outburst that produced the 13 kpc shock is reduced, since the cavity size is slightly increased by the current outburst. The presence of a second outburst reduces the outburst age in the fiducial model by about 10% to 11 Myrs.

With the above set of parameters, we find the gas density and gas temperature profile shown in Fig. 14. The figure shows the central hot, low density cocoon which acts as the piston. Just beyond the piston is the over-pressurized shell extending to about 4 kpc. In our simple one dimensional model, the presence of an existing cavity at the onset of the second

⁶ We note that there is an indication of a third weak intermediate age outburst with a surface brightness enhancement at $\sim 1'$ (see Fig. 3) but we have not modeled this weak feature.

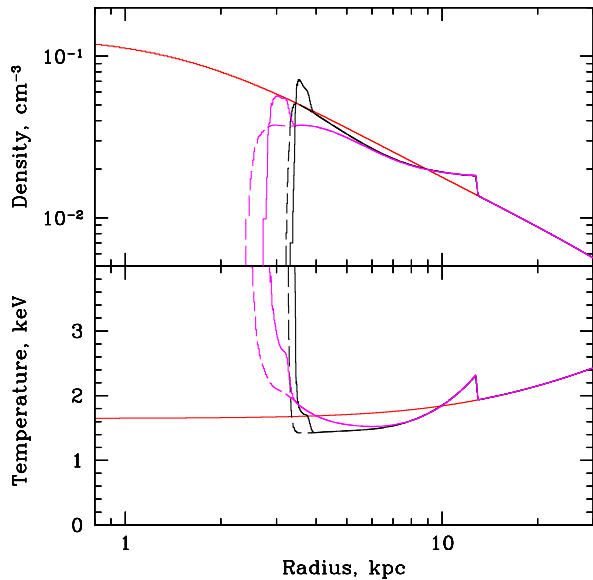


Figure 14. Comparison of models with one and two outbursts. We compare two single outburst models with energies of $E_{tot} = 5.5 \times 10^{57}$ ergs but with long (2.2 Myr) and short (0.4 Myr) durations to models with a second outburst of cumulative energy 2×10^{57} ergs and duration 1 Myr that is still ongoing. The models, with differing ages, are shown at the times when the modeled shock reaches 13 kpc, the radius of the observed shock. The single outburst models are shown with dashed lines. The outburst models with a short primary outburst are in magenta and those with long outbursts are in black. The addition of a second outburst injects energy into the existing cavity and makes only a small change to the predicted profiles. To match the observations, the age of the main outburst must be reduced to 11 Myr, while its energy is unchanged.

outburst reduces the effects of an initial short period of strong shock heating that might otherwise be present at the beginning of the second outburst. In 3D, if given sufficient time between outbursts, the second outburst will encounter a denser environment as the low density plasma rises buoyantly and is displaced by denser plasma. For short intervals between outbursts, subsequent outbursts will have the effects of their initial expansion mitigated by residual, low density plasma.

2.8. The Central Piston

The only large cavity that is seen interior to the 13 kpc shock is the central cavity, the radio cocoon (Fig. 1b and 2b). Hence, this ~ 3 kpc bubble (equivalent 1D size of the 3D bubble) of relativistic plasma must be the piston that drove the 13 kpc shock. However, since the relativistic plasma is buoyant, it will tend to bifurcate into a dumbbell shape and each half will buoyantly rise. Is the presently observed cavity surrounding the M87 nucleus and the jet consistent with having been created about ~ 11 Myr ago when the shock, presently seen at 13 kpc, was first created? Churazov et al. (2001) simulated the rise of buoyant bubbles in the M87/Virgo system. They found a buoyant velocity over a wide range of radii of about half the sound speed, $v_b \sim c_s/2$. In the M87 core, the gas temperature is about 1 keV, giving a terminal buoyant velocity of about 250 km s^{-1} . Over a time $t_b \sim 11\text{--}12$ Myr, the age of the 13 kpc shock, the initial bubble will be pinched, form an elongated (possibly dumbbell-like) shape and rise buoyantly to a distance $d_b \sim v_b t_b$. The bubble system, at present, would therefore have dimensions $\sim 3 \times 8$ kpc, consistent with the highly inclined jet angle with respect to the line of sight (Biretta et al. 1999, Wang & Zhou 2009) and consis-

tent with the 3D simulations presented in the next section (see Figs. 15 and 16).

2.9. 3D Model of the AGN Outburst

To test the sensitivity of our results to the simplifying assumption of spherical symmetry, we performed 3D jet simulations to replicate approximately the setup used in our 1D calculations.

Our simulations include a jet driven at a power of $L_{jet} = 1.2 \times 10^{44} \text{ ergs s}^{-1}$ for $\Delta t_{jet} = 2 \times 10^6$ yrs into a β -model atmosphere. Simulations were performed using the FLASH2.4 hydro code, using the PPM solver (Fryxell et al. 2000), and following the same setup described in Heinz et al. (2006) and Morsony et al. (2010). Simulations were run with a central resolution of 50 pc and used AMR to focus computational resources on the volume around the jet axis.

The simulations inject two oppositely directed jets, with the jet axis random-walking within a cone of half-opening angle of ten degrees, following the so-called dentist drill model (Scheuer 1982).

Consistent with the general model employed in this paper, the expanding lobes excavate two cavities that drive an elliptical shock, the semi-major axis of which is aligned with the mean jet direction. The radio cocoon structure has a reasonable shape compared to typical central cluster radio sources, with an aspect ratio of approximately 3:1.

Simulations were run until the semi-minor axis of the shock reached the measured shock size in M87 of 13 kpc. A density slice through the jet axis is shown in Fig. 15, showing the under-dense radio lobes and the shock. The aspect ratio of the shock is approximately 1.3:1.

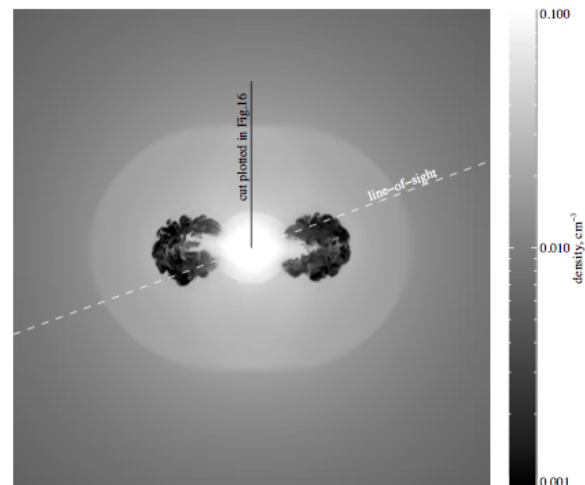


Figure 15. Density slice through 3D simulation of the jet-driven shock in M87 (see §2.9 for details of the setup).

The jet viewing angle in M87 is likely close to the line of sight (e.g., Biretta et al. 1999, Wang & Zhou 2009). Thus the elongation of the shock is likely hidden by projection. It is therefore appropriate to use measurements of the shock properties along the semi-minor axis in the simulation for comparisons with observations and the 1D models. Because an elongated shock requires a larger energy (roughly by the aspect ratio of 1.3) compared to a spherical shock, we used a larger total injected energy of $E_{jet} = L_{jet} \Delta t_{jet} = 7.4 \times 10^{57} \text{ ergs} =$

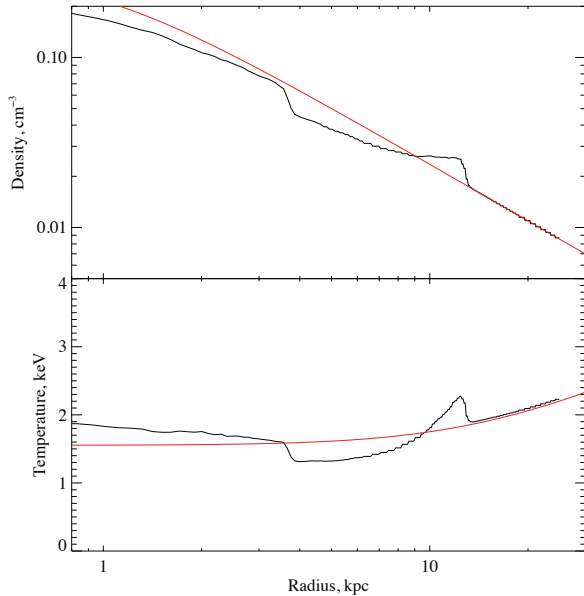


Figure 16. Density and temperature profiles along the semi-minor axis of the shock in the 3D simulations shown in Fig. 15. The “edge” feature seen at ~ 4 kpc is produced by emission from gas that has refilled the volume (visible as light region in Fig. 15) behind the expanding piston (visible as a dark region in Fig. 15). The depression in density that extends to ~ 8 kpc arises from the lower density plasma in the expanding cocoon along the line of sight. The decrease in temperature behind the shock is the characteristic of weak shocks discussed in Fig. 7.

$1.3 \times E_{1D}$.

The radial density and temperature profiles along the semi-minor axis of the shock are plotted in Fig. 16. Outward of the 1D piston location, they agree well with the profiles plotted in Fig. 5 for our fiducial 1D model. In particular, the density and temperature jumps at the shock agree well with the 1D model, supporting the use of these measurements as observational diagnostics. The simulations also show a low-temperature post-shock region between 3.5 kpc and the shock, as predicted by the 1D fiducial model. Furthermore, the 3D model reproduces the distinguishing characteristic of the piston-driven expansion: the absence of a large increase in temperature outside the piston (and interior to the shock) that would be produced by impulsive (instantaneous) energy injection in a Sedov-like mode. We note again that this relies on the assumption that thermal conduction is negligible.

The main difference between our 1D and 3D models is the presence of *two* off-center pistons in the 3D case, which leads to the elongation of the shock. The central region in the simulation is re-filled by gas that falls back and generates a new (slightly hotter) core after the jet is turned off.

It is straightforward to understand why the 1D model is so successful in reproducing the properties of the 3D simulations in the direction perpendicular to the jet: The lateral expansion of a cocoon-driven shock is energy (i.e., pressure) driven, while the initial longitudinal expansion of the shock is driven by the momentum of the jet, as argued by Begelman & Cioffi (1989). The only correction required between 1D and 3D is therefore the total volume of the shock, which increases the energy (by about 30%) required to drive a shock to a given semi-minor axis by the shock aspect ratio, as confirmed by our simulations.

3. CONCLUSION

Hot gaseous atmospheres are ideal tracers of major events in the evolution of brightest cluster (or group) galaxies (BCGs), their central supermassive black holes (SMBHs), and their dark matter halos. In addition to evidence of outbursts, X-ray images and temperature maps provide constraints on gas mixing from mergers through shocks, cold fronts, and “gas sloshing” (e.g., Markevitch & Vikhlinin 2007; Markevitch, Vikhlinin & Mazzotta 2001, Markevitch et al. 2002; Markevitch, Markevitch & Murray 2001; Johnson et al. 2010). Abundance distributions also show evidence for gas motions and merging events (e.g., Rebusco et al. 2005, 2006; Xiang et al. 2009; Simionescu et al. 2010). Another ICM tracer of the dynamic history is encoded in the X-ray surface brightness fluctuations (Churazov et al. 2012, Zhuravleva et al. 2014). For M87, the obvious outburst history extends over about 100 Myrs. Our discussion above has concentrated on the outburst that produced the nearly circular shock at 13 kpc and the central “bubble” whose inflation drove the shock into the surrounding atmosphere. The relatively simple geometry of the system provided the opportunity to explore the details of the outburst and yielded quantitative estimates of the outburst properties including its age, $\tau \sim 11 - 12$ Myrs, its energy, $E_{tot} \sim 5 - 6 \times 10^{57}$ ergs, and duration, $\Delta t \sim 1 - 3$ Myrs. In addition, we are able to estimate the present epoch energy partition with about 80% of the energy available for heating the gas and about 20% carried away, beyond 13 kpc, by the shock as it weakens to a sound wave (see Table 1). Thus, during the outburst, in the fiducial model, about 30% of the outburst energy is deposited in the shock. In this model, $\sim 10\%$ of this energy has already been dissipated into heat as the shock traversed the region interior to its present 13 kpc location, while the remaining $\sim 20\%$ is carried to larger radii. For M87, a large fraction of the outburst energy resides in the central bubble enthalpy. As Churazov et al. (2001, 2002) argued, the bulk of this energy is converted to thermal energy of the X-ray emitting gas in the central region surrounding M87.

In the context of our simple model, we also are able to estimate the properties of the current, ongoing outburst that has only slightly altered the signature left by the preceding outburst. The signature of the current outburst is consistent with having begun about 1 Myr ago and having injected 2×10^{57} ergs into the preexisting cavity. As noted above, the $\sim 11 - 12$ Myr old outburst inflated a cavity that is now elongated, at least partially by buoyancy. While the exact values describing the M87 outbursts are uncertain, with the outburst energy somewhat larger than the 1D model predicts (see section 2.9 and the discussion of the 3D model), the qualitative description of a “slow” (few Myr) outburst remains valid and is confirmed by the more realistic 3D model.

M87 provides a view of a “typical” outburst from a low-Eddington rate accretor with the bulk of the energy liberated as mechanical, rather than radiative, energy. Considerable attention has been given to the very energetic outbursts in luminous clusters (e.g., Nulsen et al. 2005) and to some of the spectacular outbursts in groups (e.g., NGC5813; Randall et al. 2011). However, luminous early type galaxies also have hot coronae (Forman, Jones & Tucker 1985) and, like their more luminous cousins, also harbor mini-“cooling cores”. In the absence of any heating, these systems would have mass deposition rates up to a few solar masses per year (Thomas et al. 1986) and yet they host very little star formation and remain “red and dead” (e.g., Hogg et al. 2002). Outbursts very similar to those discussed for M87 are also present in these

systems. NGC4636 (Jones et al. 2002, Baldi et al. 2009), M84 (Finoguenov et al. 2008), and NGC4552 (Machacek et al. 2006) are representative examples of this class.

There are a variety of energy sources suitable for replenishing the radiated energy from the hot gas in galaxy cluster cores. Two of the most prominent are mergers and AGN outbursts which drive gas motions. In M87, we see effects of both processes, e.g., a) ongoing mergers such as M86 (Forman et al. 1979, Randall et al. 2008) and gas sloshing of the entire Virgo core (Simionescu et al. 2010) and b) AGN outbursts from M87 as we have discussed in detail above that inflate buoyant bubbles. In the context of gas sloshing, ZuHone et al. (2010) have discussed the mixing of hotter gas from larger radii with cooler gas from the central regions of the cluster (or galaxy). The mechanism for converting the bulk motions to heat has only recently been probed. Zhuravleva et al. (2014) argued that gas motions, that arise from both merging and SMBH feedback (primarily, motions driven by the rise of buoyant plasma bubbles as discussed for M87 above), are very likely converted to thermal energy via dissipation of turbulence. The turbulent heating inferred for M87 (and Perseus) is sufficient to balance the radiative cooling. Hence, we can now begin to quantitatively understand the feedback process and conversion of gas motions to thermal energy of the gaseous atmosphere.

The outbursts from M87 are characteristic of radiatively inefficient accretion (e.g., Ichimaru 1977, Rees et al. 1982, Narayan & Yi 1994, Abramowicz et al. 1995, Blandford & Begelman 1999, Yuan & Narayan 2014). Early-type galaxy

evolution models that include both radiative and mechanical feedback have been explored extensively. Pellegrini, Ciotti & Ostriker (2012, and references therein) have modeled the evolution of isolated early type galaxies over cosmological times. They find episodic outbursts with high quasar-like radiative luminosities ($\sim 10^{46}$ ergs s^{-1}) at early epochs. M87, and most present epoch early-type galaxies, lie in richer environments (cluster or group centers or cluster cores). Although the gas environment is much richer, present epoch early-type galaxies appear to have more moderate outbursts than those at earlier epochs. Future X-ray missions will be able to study the detailed properties of outbursts and probe the conversion of bulk motions to thermal energy (e.g., Croston et al. 2013, Vikhlinin 2012). The ability to probe to high redshift with arc second angular resolution (Vikhlinin 2012 see section 3.1 and Fig. 3) could fully test models of galaxy evolution and the impact of the SMBHs that lie in their nuclei, by tracing the evolution of both the AGN and the surrounding hot gaseous atmosphere and deriving properties (luminosity, temperature, density profile, and abundance) from redshifts of $z \sim 6$ to the present.

This work was supported by contracts NAS8-38248, NAS8-01130, NAS8-03060, the Chandra Science Center, the Smithsonian Institution, the Institute for Space Research (Moscow) and Max Planck Institute für Astrophysik (Munich). S.H. acknowledges support through NSF grant AST 1109347. We thank the anonymous referee whose comments significantly improved the paper.

REFERENCES

- Abdo, A. et al. 2009, *ApJ*, 707, 55.
 Abramowicz, M., Chen, X., Kato, S., Lasota, J., Regev, O. 1995, *ApJL*, 438, L37
 Acciari, V. et al. 2010, *ApJ*, 716, 819.
 Allen, S. W., Dunn, R. J. H., Fabian, A. C., Taylor, G. B. & Reynolds, C. S. 2006, *MNRAS*, 372, 21
 Baldi, A. et al. 2009, *ApJ* 707, 1034
 Begelman, M. & Cioffi, D. 1989, *ApJL*, 345, L21
 Bicknell, G. & Begelman, M. 1996, *ApJ*, 467, 597
 Biretta, J, Sparks, W., Macchetto, F. 1999, *ApJ*, 520, 621
 Blandford, R. & Begelman, M. 1999, *MNRAS*, 303, L1
 Brighenti, F. & Mathews, W. 2002, *ApJL*, 574, L11
 Churazov, E., Forman, W., Jones, C. & Böhringer, H. 2000, *A&A*, 356, 788
 Churazov, E., Brügggen, M., Kaiser, C., Böhringer, H. & Forman, W. 2001, *ApJ*, 554, 261
 Churazov, E., Sunyaev, R., Forman & Böhringer, H. 2002, *MNRAS*, 332, 729
 Churazov, E., Sazonov, S., Sunyaev, R., Forman, W., Jones, C. & Böhringer, H. 2005, *MNRAS*, 363, L91
 Churazov, E., Forman, W., Vikhlinin, A., Tremaine, S., Gerhard, O. & Jones, C. 2008, *MNRAS*, 388, 1062
 Churazov, E. Vikhlinin, A., Zhuravleva, I., Schekochihin, A., Parrish, I., Sunyaev, R., Forman, W., Böhringer, H., & Randall, S. 2012, *MNRAS*, 421, 1123
 Churazov, E., Arevalo, P., Forman, W., Jones, C., Schekochihin, A., Vikhlinin, A., Zhuravleva, I. 2016, *MNRAS*, 463, 1057
 Ciotti, L Ostriker, J. 2012, *ASSL*, 378, 83
 de Gasperin et al. 2012, *A & A*, 547, 56
 Croston, J. et al. 2013, *arXiv*, 1306.2323
 Di Matteo, T., Allen, S., Fabian, A., Wilson, A., Young, A. 2003, *ApJ*, 582, 133
 Fabian, A. et al. 2003, *MNRAS*, 344, L43
 Fabian, A. 2012, *ARA&A*, 50, 455
 Fabian, A., Sanders, J., Taylor, G., Allen, S., Crawford, C., Johnstone, R. & Iwasawa, K. 2006, *MNRAS*, 366, 417
 Finoguenov, A., Ruszkowski, M., Jones, C., Brügggen, M., Vikhlinin, A. & Mandel, E. 2008, *ApJ*, 686, 911
 Ford, H. et al. 1994, *ApJL*, 435, L27
 Forman, W., Schwarz, J., Jones, C., Liller, W. & Fabian, A. 1979, *ApJL*, 234, L27
 Forman, W., Jones, C. & Tucker, W., 1985, *ApJ*, 293, 102
 Forman, W., Nulsen, P., Heinz, S., Owen, F., Eilek, J., Vikhlinin, A., Markevitch, M., Kraft, R., Churazov, E. & Jones, C. 2005, *ApJ*, 635, 894
 Forman, W., Jones, C., Churazov, E., Markevitch, M., Nulsen, P., Vikhlinin, A., Begelman, M., Böhringer, H., Eilek, J., Heinz, S., Kraft, R., Owen, F., & Pahre M. 2007, *ApJ*, 665, 1057
 Fryxell, B., Olson, K., Ricker, P. Timmes, F., Zingale, M., Lamb, D., MacNeice, P., Rosner, R., Truran, J. & Tufo, H., 2000, *ApJS*, 131, 273
 Gebhardt, K., Adams, J., Richstone, D., Lauer, T., Gültekin, K., Murphy, J. & Tremaine, S. 2011, *ApJ*, 729, 119
 Harms, R. J., et al. 1994, *ApJ*, 435, L35
 Harris, D., Biretta, J., Junor, W., Perlman, E., Sparks, W. & Wilson, A., 2003, *ApJL*, 586, L41
 Harris, D., Cheung, C., Biretta, J., Sparks, W., Junor, W., Perlman, E. & Wilson, A., 2006, *ApJ*, 640, 211
 Heinz, S., Brügggen, M., Young, A. & Levesque, E. 2006, *MNRAS*, 373, L65
 Hines, D., Owen, F. & Eilek, J. 1989, *ApJ*, 347, 713
 Hogg, D. et al. 2002, *AJ*, 124, 646
 Hugoniot, H. 1887, *Journal de l'Ecole Polytechnique* 57, 3
 Ichimaru, S. 1977, *ApJ*, 214, 840
 Johnson, R. Markevitch, M., Wegner, G., Jones, C. & Forman, W. 2010, *ApJ*, 710, 1776
 Jones, C., Forman, W., Vikhlinin, A., Markevitch, M., David, L., Warmflash, A., Murray, S. & Nulsen, P. 2002, *ApJL*, 567, L115
 Landau, L. D., & Lifshitz, E. M. 1959, *Fluid Mechanics* (London:Pergamon)
 Machacek, M., Nulsen, P. E. J., Jones, C. & Forman, W. R. 2006, *ApJ*, 648, 947
 Macchetto, F., Marconi, A., Axon, D. J., Capetti, A., Sparks, W., & Crane, P. 1997, *ApJ*, 489, 579
 Markevitch, M. & Vikhlinin, A. 2007, *PhR*, 443, 1
 Markevitch, M., Gonzalez, A, David, L., Vikhlinin, A., Murray, S., Forman, W., Jones, C. & Tucker, W. 2002, *ApJL*, 567, L27
 Markevitch, M., Vikhlinin, A. & Mazzotta, P. 2001, *ApJL*, 562, L153
 Markevitch, M., Vikhlinin, A. & Murray, S. 2001, *ApJ*, 551, 160
 Marshall, H., Miller, B., Davis, D., Perlman, E., Wise, M., Canizares, C., Harris, D. 2002, *ApJ*, 564, 683
 McNamara, B. R., Nulsen, P. E. J., Wise, M. W., Rafferty, D. A., Carilli, C., Sarazin, C. L., Blanton, E. L. 2005, *Nature*, 433, 45

- Morsony, B., Heinz, S., Brüggén, M. & Ruszkowski, M. 2010, *MNRAS*, 407, 1277
- Million, E. T., Werner, N., Simionescu, A., Allen, S. W., Nulsen, P. E. J., Fabian, A. C., Böhringer, H. & Sanders, J. S. 2010, *MNRAS*, 407, 2046
- Moscibrodzka, M., Falcke, H., Shiokawa, H. 2016, *A&A*, 586, 38
- Narayan, R. & Yi, I 1994 *ApJ*, 428, L13
- Nulsen, P., McNamara, B., Wise, M. & David, L. 2005, *ApJ*, 628, 629
- Nulsen, P. E. J., Jones, C., Forman, W. R., David, L. P., McNamara, B. R., Rafferty, D. A., B  rzan, L. & Wise, M. W. 2007, Heating versus Cooling in Galaxies and Clusters of Galaxies, *ESO Astrophysics Symposia* (eds. B  hringer, Pratt, Finoguenov, Schuecker: Springer-Verlag Berlin Heidelberg) 210
- Owen, F., Eilek, J. & Kassim, N. 2000, *ApJ*, 543, 611
- Pellegrini, S., Ciotti, L. & Ostriker, J. 2012, *ApJ*, 744, 21
- Prieto, M. A., Fernandez-Ontiveros, J. A., Markoff, S., Espada, D., Gonzalez-Martin, O. 2016, *MNRAS*, 457, 3801
- Randall, S. W., Forman, W. R., Giacintucci, S., Nulsen, P. E. J., Sun, M., Jones, C., Churazov, E., David, L. P., Kraft, R., Donahue, M., Blanton, E. L., Simionescu, A. & Werner, N. 2011, *ApJ*, 726, 86
- Randall, S., Nulsen, P., Forman, W., Jones, C., Machacek, M., Murray, S. & Maughan, B. 2008, *ApJ*, 688, 208
- Rankine, W. 1870, *Phil. Trans. Roy. Soc.*, 160, 277
- Rebusco, P., Churazov, E., B  hringer, H. & Forman, W. 2005, *MNRAS*, 359, 1041
- Rebusco, P., Churazov, E., B  hringer, H. & Forman, W. 2006, *MNRAS*, 372, 1840
- Rees, M. J., Begelman, M. C., Blandford, R. D. & Phinney, E. S. 1982, *Nature*, 295, 17
- Reynolds, C., Di Matteo, T., Fabian, A., Hwang, U & Canizares, C. *MNRAS*, 1996, 283, L111
- Scheuer, P. 1982 in *IAU Symp. 97: Extragalactic Radio Sources* (eds. D. Heeschen & C. Wade), 163-165
- Shi, Y, Rieke, G., Hones, D. Gordon, & K. Egami, E. 2007, *ApJ*, 655, 781
- Simionescu, A. et al. 2010, *MNRAS*, 405, 91
- Stawarz, L., Aharonian, F., Kataoka, J., Ostrowski, M., Siemiginowska, A., Sikora, 2006, *MNRAS*, 370, 981
- Tang, X. & Churazov, E. 2017, *arXiv* 170105231
- Thomas P. A., Fabian A. C., Arnaud K. A., Forman W., Jones C., 1986, *MNRAS*, 222, 655
- Vikhlinin, A., Markevitch, M., Murray, S. 2001, 555, L87
- Vikhlinin, A., Reid, P., Tananbaum, H., Schwartz, D. A., Forman, W. R., Jones, C., Bookbinder, J., Cotroneo, V., Trolier-McKinstry, S., Burrows, D., Bautz, M. W., Heilmann, R., Davis, J., Bandler, S. R., Weisskopf, M. C. & Murray, S. S. 2012, *SPIE*, 8443, 16
- Walsh, J., Barth, A., Ho, L. & Sarzi, M. 2013, *ApJ*, 770, 86
- Wang, C-C. & Zhou, H-Y. 2009, *MNRAS*, 385, 301
- Xiang, F. et al. 2009, *MNRAS*, 398, 575
- Yuan, F., Yu, Zhaolong, Ho, Luis C. 2009, *ApJ*, 703, 1034
- Yuan, F. & Narayan, R. 2014, *ARA&A*, 52, 529
- Zeldovich, Y & Razier, Yu. 2002, *Physics of Shock Waves and High Temperature Hydrodynamic Phenomena* (New York: Dover), pp. 99-101
- Zhuravleva, I., Churazov, E., Schekochihin, A. A., Allen, S. W., Arevalo, P., Fabian, A. C., Forman, W. R., Sanders, J. S., Simionescu, A., Sunyaev, R., Vikhlinin, A. & Werner, N. 2014, *Nature*, 515, 85
- ZuHone, J. Markevitch, M. & Johnson, R. 2010, *ApJ*, 717, 908